GSA Data Repository 2019297

Rose, C.V., et al., 2019, Insights into past ocean proxies from micron-scale mapping of sulfur species in carbonates: Geology, https://doi.org/10.1130/G46228.1

SUPPLEMENTARY ONLINE MATERIAL

Samples

Sedimentary rocks of the Ordovician-Silurian Anticosti Basin represent a subtidal, storm-influenced, carbonate ramp-platform (Petryk, 1981; Long and Copper, 1987; Sami and Desrochers, 1992; Long, 2007; Desrochers et al., 2010). The basin developed on top of Grenville-age crust on the eastern margin of Laurentia. The long axis of the island is oblique to the reconstructed paleo-shoreline, with the west end of the island occupying a more distal position (Petryk, 1981). Previous stratigraphic work has established several cycles of (glacio)-eustatic sea level fluctuations in the Vaureal and Ellis Bay Formations, interpreted to reflect the waxing and waning of continental ice sheets on Gondwana (Desrochers et al., 2010). Subsidence of the Anticosti Basin accommodated an almost uninterrupted succession of mixed carbonate-siliciclastic strata deposited across the Ordovician-Silurian boundary despite large glacioeustatic changes in base level (Petryk, 1981; Long, 2007). Discontinuities in the $\delta^{13}C_{carb}$ record across lithostratigraphic boundaries, however, suggest that the basin experienced intermittent hiatuses in deposition during the Hirnantian Stage (Jones et al., 2011).

Sections were logged and sampled through the Ellis Bay and lower Becscie Formations during the summers of 2008 and 2009 (Jones et al., 2011). Carbonate hand sample (908-ONC), an oncoid grainstone from the Ellis Bay Formation, was cut and polished to remove weathering rinds and made into 1 inch-round, 30 μm-thick thin sections for analyses. This sample comes

from the oncoid platform bed (OPB), a marker bed deposited during sea-level lowstand associated with the Hirnantian glaciation and which can be traced and correlated across Anticosti Island. An additional sample (908-1.0) has been included to demonstrate sulfate and sulfide distributions across different textures (Fig. DR3). This richly fossiliferous crinoidal packstone is from lower down in the stratigraphy in the Lousy Cove Mb, well before the onset of the Hirnantian isotopic excursion. Detailed descriptions of facies can be found in Jones et al. (2011).

Synchrotron-based sulfate concentrations were determined by calibration using calcite crystals precipitated in the laboratory under controlled growth conditions with varying amounts of sulfate. Optically clear calcite crystals were grown using a free drift method modified after (Gruzensky, 1967; Paquette and Reeder, 1990). Glass beakers containing unseeded solutions of $CaCl_2$ and NH_4Cl were sealed from the laboratory atmosphere, and the sealed atmosphere was exposed to solid $(NH_4)_2CO_3$, which decomposes at room temperature to form $CO_2(g)$ and $NH_3(g)$. As these gases diffuse into the solutions, pH (controlled by inorganic carbonate and ammonia equilibria) increases, which yields CO_3^{2-} and HCO_3^- that react with Ca^{2+} to form calcite. Calcite nucleation occurred within 1-2 days, and crystal growth proceeded for an additional 15-20 days until pH remained constant and the experiments were terminated. Sulfate was co-precipitated with the calcite by introducing concentrated Na_2SO_4 solutions of varying concentration after nucleation (Staudt et al., 1994). Sulfate concentrations were determined based on the replicate ion chromatography (IC) measurements of dissolved crystals and correspond to concentrations (± 3%) of 23400 ppm, 4900 ppm, and 0 ppm. These crystals were analyzed at the Advanced Photon Source (APS) and Stanford Synchrotron Radiation Lightsource (SSRL) and used to calibrate the resulting sulfate concentrations measured in these samples.

Carbonate Petrography

The oncoid grainstone (908-ONC) consists of gastropod, brachiopod, bivalve, ostracode, crinoid and other echinoderm fragments throughout the sample (Fig. DR1). The thin section also includes trepostome and cryptostome bryozoans and dasyclad algae (Fig. DR2) and amorphous grains with micrite coatings. The centers of the gastropods contain syndepositional detrital material and the internal shell structure of the brachiopod fragments is still visible. Micritization and neomorphism created micrite coatings around many of the shell fragments. The originally aragonitic shell of the gastropods subsequently dissolved and was replaced by later calcite cement, leaving molds of the shell morphology. Throughout the thin section, there are examples of micritic coatings, micrite infill in the interior of gastropods, micritic envelopes progressing to micritized grains, as well as irregular shaped grains such as peloids, intraclasts, and microbial micrite associated with oncoids. There are two generations of sparry cement; there is an early marine relict cement with small scalenohedral crystals on the underside of bivalve and gastropod shells, often with micritized terminations, that is not developed on all surfaces, and there is a later coarse spar occluding remaining porosity. To demonstrate the utility of this approach across a range of different textures, we also quantified and mapped sulfate and sulfide distributions in a crinoidal packstone (908-1.0) (Fig. DR3). This richly fossiliferous packstone consists of predominantly crinoid fragments but also includes gastropod, brachiopod, and bivalve fragments. These skeletal grains often have micritized rims and show evidence for an early marine cement and later coarse spar that occludes porosity.

Advanced Photon Source (APS)

X-ray fluorescence (XRF) maps and S K-edges XAS data were collected at the

GeoSoilEnviroCARS (GSECARS) micro-probe beamline 13-ID-E at the Advanced Photon Source (APS) at Argonne National Laboratory. The APS is a 7 GeV APS electron storage ring running at 102 mA and beamline 13-ID-E utilizes a 3.6 cm period undulator X-ray source. A liquid nitrogen cooled, Si(111) double-crystal monochromator was used to select X-rays of the desired energy, and this monochromatic beam was focused to ~ 2x2 μm using Kirkpatrick-Baez focusing mirrors. At the S K-edge (2472 eV), the flux at the sample was approximately $5x10^{10}$ photons s^{-1}. Although the Kirkpatrick-Baez mirrors, using bare silicon to focus the beam, provide excellent harmonic rejection, the focusing configuration was slightly modified to allow a small amount of 3rd harmonic intensity (X-rays with energy 7400 eV) to deliberately allow for inefficient excitation elements between S and Fe. Monochromator calibration provides excellent agreement with refined absorption edge energies measured by Kraft et al. (1996) over the range of energies accessible at 13-ID-E for spectroscopy.

X-ray fluorescence was measured with a Vortex ME-4 silicon drift-diode detector array (SII NanoTechnology USA Inc.) with digital signal processing electronics from XIA. The sample and path for incident beam and for fluorescence from sample to the detector was kept in a bag purged with helium to reduce attenuation of the X-rays by air. XRF mapping was done in a continuous scan mode, collecting full XRF spectra at 30 to 100 msec intervals. Integrated counts within energy regions of the XRF spectrum corresponding the Kα emission lines for S, Ca, Mn, and Fe were extracted from the full spectra at each point to make maps of elemental distribution. Measured intensities were corrected for detector deadtime.

Sulfur K-edge spectra were collected by scanning the incident beam from 2450-2468 eV in 2 eV steps, 2468-2485 eV in 0.1 eV steps and from 2485-2550 eV in 2 eV steps at 2 seconds per energy point. To visualize the sulfur speciation at every pixel, rather than solely at discrete XAS

90 points, and because the sharp resonance for sulfate is so intense and resolved, XRF maps were
91 made at 3 separate energies: well above the S K edge (at 2520 eV); at the sulfate resonance (at
92 2481.5 eV); and at the peak corresponding to sulfide phases (at 2471 eV) to separately map total
93 sulfur, sulfate, and sulfide components.
94 A $CaSO_4$ standard provides a white line maximum at an energy of ~2481.5 eV. Pyrrhotite
95 measured at 13-ID-E displays a pronounced spectral peak with a maximum at ~2469.8 eV. These
96 values are ~1 eV lower than reported in previous studies (e.g., Jugo et al., 2010), which we
97 attribute to differences in monochromator calibration. For purposes of comparison between
98 results at different facilities, here we have adjusted the APS energies up by ~1 eV to align the
99 sulfate white line energies to those obtained at the Stanford Synchrotron Radiation Lightsource
100 (SSRL).
101
102 **Stanford Synchrotron Radiation Lightsource (SSRL)**
103 X-ray fluorescence images were collected at the Stanford Synchrotron Radiation Lightsource
104 (SSRL) using beam line 14–3 with the Stanford Positron Electron Accelerating Ring (SPEAR)
105 containing 500 mA at 3.0 GeV. For X-ray fluorescence imaging, the incident X-ray energy was
106 set to energies around the sulfur absorption edge (2472 eV) using a Si (111) double crystal
107 monochromator. The monochromator energy was calibrated by setting the first thiol peak of a
108 sodium thiosulfate powder to 2472.02 eV. At the S K-edge (2472 keV), the flux at the sample
109 was approximately $2x10^{10}$ photons s^{-1}. The fluorescence lines of the elements of interest, as well
110 as the intensity of the total scattered X-rays, were monitored using a Vortex silicon drift diode
111 detector (SII NanoTechnology USA Inc.) with Xspress3 digital signal processing electronics
112 from Quantum Detectors. In addition to these regions of interest, the entire fluorescence

spectrum was also collected at each data point. The microfocused beam of 5x5 μm was provided by a Cr-coated Kirkpatrick-Baez mirror pair (Xradia Inc.) The incident and transmitted X-ray intensities were measured with helium-filled ion chambers. Samples were mounted at 45° to the incident X-ray beam and were spatially rastered in the microbeam using a Newport VP-25XL-XYZ stage in a helium purged sample chamber. Beam exposure was typically 50 ms per pixel. At specific points of interest, the full X-ray absorption spectrum was collected. The spectrum was collected from 2460 eV to 2510 eV using 0.25 eV steps, and from 2510 eV to 2600 eV using 1 eV steps. For examining the detailed sulfate speciation, the region between 2475 and 2490 eV was oversampled at finer energy steps, 0.05 eV.

All XAS data were processed using standard methods in SIXPACK (Webb, 2005). Briefly, data were background subtracted using a linear pre-edge region (up to 2465 eV) and a linear post-edge (after 2510 eV). Processing of XRF maps was performed in the MicroAnalysis Toolkit (Webb, 2011). Images were corrected as needed for incident intensity variations and then the data was smoothed using a 5x5 Gaussian kernel with a 0.80 pixel FWHM to improve counting statistics and signal to noise. To determine the amount of sulfide and sulfate, data images of the sulfur at the three incident energies were subsequently fit at every pixel in a least-squares sense to the intensities of sulfide and sulfate standards at the incident energies of each data image. This fitting separates the data into counts of each sulfur species. Counts were converted to concentrations by calibration of signal counts using a series of calcite CAS standards of known sulfate concentration.

Discussion of S Spectra

XAS S K-edge spectra of standard compounds, including organic thiols, sulfoxide, sulfonates, sulfate ester, and inorganic sulfate are shown in Fig. 1. Note that species in which the sulfate moiety has a distorted tetrahedral symmetry shift to lower energy, which can lead to strong asymmetry profiles and splitting of the peak intensities. It is important to note in these cases that the inorganic sulfate (e.g., gypsum) has the same peak energy for the sulfate peak as protamine sulfate, which is an ionic form of sulfate to an organic counter ion. Since the sulfates in both cases are inorganic ionic forms, the sulfate peak position is the same. The major difference in this case is the post-edge structure of the gypsum, which shows resonances that occur in the 20 eV following the sulfate peak which are present primarily in crystalline inorganic sulfates with divalent counter-ions and absent in the protamine organic counter-ion case (Tamenori et al., 2014). In contrast, when protonated sulfate (sodium bisulfate) or sulfate esters (chondroitin sulfate) are measured, the sulfate peak has extra intensity at slightly lower energies. A stronger asymmetry, as in the ester vs. protonated case, leads to a stronger observed split in the peak. The strong sulfate transition can be assigned to the nature of the 3p holes in the sulfate electronic structure, which are triply degenerate. The increase in the p vacancies also enhances the intensity of the 1s to 3p dipole allowed transition (Evans, 2018). The observed split in the sulfate transitions in the above cases is due to the change of symmetry breaking the degeneracy of the lowest unoccupied molecular orbital in sulfate.

The observed spectra of the sulfur in CAS show three characteristic spectra in the sulfate region. These are (1) the undistorted sulfate, as in the sulfates with inorganic and organic counter cations; (2) a slightly distorted sulfate, which has a peak in the sulfate region ~0.2 eV shifted to lower energy; (3) a sulfate with a strong component of the sulfate esters, displaying a strong shoulder around 2481.4 eV. There are several possible interpretations for the nature of the

158 distorted sulfate, for example, it may arise as a result of the complexation of sulfate to transition
159 metal ions, which has been shown to hybridize to the *3d* orbitals and shift the energy of the
160 sulfate peak (Okude et al., 1999). The most likely metals in these carbonate rocks would be Fe
161 and Mn. However, there does not appear to be any correlation between the presence/absence of
162 Mn/Fe and the shifted sulfate species. A second possibility could be different crystalline
163 structures of the carbonates in which the sulfate is associated. The different densities of calcite,
164 aragonite and dolomite changes the lattice parameters of the carbonates, altering the space
165 available for CAS to substitute for carbonate ions. Fernandez-Diaz et al. (2010) modeled the
166 availability of sulfate to substitute into several carbonates, showing that the denser structures
167 created larger distortions in the carbonate lattice. While the presence and preservation of
168 aragonite in Ordovician age sediments is highly unlikely and XRD analyses fail to provide
169 supporting evidence (Balthasar et al., 2011), the partial substitution of Mg for Ca in the lattice
170 could also create similar lattice contractions. This is consistent with patterns of co-occurrence of
171 sulfate and Mg in modern carbonate skeletons (Perrin et al., 2017; Cusack et al., 2008). Further
172 characterization of careful CAS control spectra will be needed to differentiate the true nature of
173 the distorted sulfate.
174
175 **Pathways for potential alteration of CAS isotopic signatures**
176 Primary CAS reflects the ambient sulfate pool from which the carbonate is first formed
177 (seawater or porewater). In principle, deviation of $\delta^{34}S_{CAS}$ values from seawater sulfate may
178 occur in marine carbonates during deposition as a result of early diagenesis (i.e., carbonate
179 cementation associated with chemically evolved porewaters), or during later-stage alteration. For
180 example, syndepositional alteration can arise if there is substantial carbonate precipitation

occurring where the isotopic composition of the local sulfate pool has been impacted by microbial metabolic activity, altering the $\delta^{34}S_{SO4}$ composition of sedimentary pore fluids. Therefore, it is possible to have primary CAS in sedimentary cements that is divergent from seawater (e.g., because it precipitated within the zone of microbial sulfate reduction). The impact of this syndeposition alteration will scale with the percent abundance of this carbonate cement within the sample, as well as the deviation of porewater $\delta^{34}S_{SO4}$ from overlying seawater. Records of $\delta^{34}S_{CAS}$ can also be compromised by late-stage diagenetic alteration associated with the migration of fluids (e.g., meteoric fluids or basinal brines) with a $\delta^{34}S_{SO4}$ composition different from seawater at the time of deposition. Therefore, it is possible to have non-primary CAS that is identical to seawater (e.g., in dolomites that form from open system flushing of high volumes of seawater). These late-stage alteration pathways have been extensively studied as to their impact on $\delta^{13}C_{carb}$, $\delta^{18}O_{carb}$, and trace element data in carbonates (Banner and Hanson, 1990; Brand and Veizer, 1981). However, only a few studies have examined the preliminary effects of diagenesis on $\delta^{34}S_{CAS}$ (Gill et al., 2008). Detailed studies have, however, observed more scatter in the $\delta^{34}S_{CAS}$ proxy than can be reconciled with it recording a primary marine signature. This scatter is found not only in bulk rock samples (e.g., Jones and Fike (2013)), but also in micro-drilled samples of individual fossils and petrographic fabrics (e.g., Present et al. (2015)). Assessing covariation of bulk-rock $\delta^{34}S_{CAS}$ data with other key bulk-rock geochemical parameters (e.g., CAS abundance, $\delta^{13}C_{carb}$, $\delta^{18}O_{carb}$, Mg, Sr, etc.) (Gill et al., 2008) provides one approach for discerning alteration. It is critical for such screening to be performed on the microscale to differentiate the fabric-specific processes effecting $\delta^{34}S_{CAS}$ in the various constitutive components of complex sedimentary carbonates.

Statistical Analysis of Synchrotron Sulfate Concentration Data

Two sectors of a single thin section were analyzed by synchrotron analysis as reported in the main text. Data for each sector consisted of pixelated sulfate concentrations from across the entire sector. Sector 1 (Fig 2: "Heart") consisted of a region 1001 by 601 pixels (5 um pixel size), while Sector 2 (Fig 3: "Anvil") was 601 by 601 pixels. Regions of Interest (ROIs) were defined within each sector by comparing the synchrotron data to the component data inferred from optical petrography. Each ROI was targeted to recover sulfate concentrations from a particular component of the thin section. The targeted components were: skeletal grains, non-skeletal grains, cements, detrital micrite, micritic coatings, or oncoids. ROIs ranged in size from 220 pixels to 6723 pixels.

To visualize the distribution of pixel-by-pixel sulfate concentrations within each ROI, we produced a normal probability (Normal QQ) plot for each ROI (Fig. DR4). These plots show that while data from many ROIs can be well modeled by a normal distribution (where QQ plot shows a near-linear correspondence between theoretical and sample probability distributions), sulfate concentration distributions in other ROIs show large deviations from normality. Notched boxplots of the data from each sample are presented in Fig. 4. These plots show the distributions of sulfate concentrations from each ROI and suggest that the non-normal distribution of concentration in some ROIs is largely a consequence of a natural limit produced when sulfate concentrations below the limit of detection are reported as 0. In each plot the box contains 50% of the data, spanning from the 25th percentile to the 75th percentile of the data. The range between the 25th and 75th percentile is the interquartile range (IQR), and the whiskers extend an additional 1.5*IQR outside the IQR. Outliers identified by the Tukey method – i.e. datapoints that fall more than 1.5*IQR beyond the interquartile range (IQR) - are plotted as points beyond

227 the end of the whiskers. The notch spans the 95% confidence interval for the median of each
228 sample. This approach facilitates rapid comparison among samples to determine whether sample
229 medians differ.

230 We analyzed sulfate concentration distributions within each ROI by assuming that they are
231 normally distributed but left-censored at zero. This was achieved by performing a maximum
232 likelihood estimation for the sulfate concentration mean and standard deviation in each ROI
233 using the *fitdistrplus* package (Delignette-Muller and Dutang, 2015) in R (R Core Team, 2016).
234 The R code is available at https://github.com/bradleylab/synchrotron_sulfur. For samples with
235 relatively high concentrations of sulfate, the maximum likelihood estimation (MLE) of the mean
236 concentration was nearly identical to the standard estimate (Table S1). However, for samples in
237 which a significant portion of the data are censored against the lower bound, the MLE produced
238 a different estimate of the mean and standard deviation. One drawback of the MLE method is
239 that it is very sensitive to outliers, and some of the ROIs have a large number of outliers (Fig. 4).
240 To reduce the influence of outliers, we re-applied the MLE method to estimate the mean and
241 standard deviation of sulfate concentration in each ROI after removing outliers. This approach
242 was successful in all but one ROI, ROI 3 (coarse spar cement). In this ROI, the unusual
243 distribution near zero prevented us from fitting a normal distribution using maximum likelihood
244 estimator. Histograms of all measured sulfate concentration data and the MLE modeled the
245 normal distribution of these data are shown in Fig. DR5. The sulfate concentrations reported in
246 the main text are the MLE means, along with their standard errors.

247 We performed pairwise t-tests between each pair of ROIs in both sectors, using the test
248 statistics from the MLE to determine whether we could observe differences in the mean sulfate
249 concentrations among various components. This approach relies on the assumption that the

250 distribution of sulfate concentrations among the pixels within each ROI are best fit by a normal
251 distribution that is truncated at the boundary condition. The results of these t-tests are reported in
252 Tables S2. The reported p-values are adjusted with the Holm method for the familywise error
253 rate deriving from multiple comparisons.

254 In comparing these p-values, it is evident that nearly all of the sample means are discernible
255 from one another. The only pair of samples for which the adjusted p-value is > 0.05 is the Sector
256 1 (Heart) pair ROI 2 and 7 (adjusted $p = 0.57$). For Sector 2 (Anvil), p-values from t-test between
257 all ROI pairs are < 0.05, with the largest value the comparison between ROIs 11 and 18 ($p =$
258 0.031). Sector 1 (Heart) ROI 3 could not be analyzed, since we could not produce MLE
259 parameters after removal of outliers, but its extreme distribution is consistent with a mean sulfate
260 concentration distinct from most other samples and very near zero.

261

262 **Mixing Models**

263 To understand how differences among components could affect the sulfate concentration of bulk
264 carbonate, we performed 3-component mixing models using the distributions measured for
265 various components. We defined six components: skeletal grains, nonskeletal grains, detrital
266 micrite, oncoids, cement, and micritic coatings. We defined an end-member sulfate concentration
267 mean and standard deviation for each component by randomly sampling 100,000 'pixels' from
268 left-censored normal distributions with means and standard deviations identical to that calculated
269 for ROIs. We then performed three-component mixing calculations to calculate the sulfate
270 concentration for bulk carbonate that consisted of any combination of three components. This
271 approach makes the fundamental assumption that sulfate concentrations are a strong function of
272 the component. In other words, the sulfate concentrations measured for example in skeletal

grains, are a function of the skeletal grains themselves and do not depend on the proportion of that component in the bulk carbonate. Increasing the proportion of a high-sulfate component in the bulk carbonate will increase the concentration of bulk sulfate in the rock.

Fig. DR6A shows a ternary diagram with the calculated sulfate concentration of bulk carbonate comprised of three components: nonskeletal grains, detrital micrite, and cement. Since two of these components (nonskeletal grains and cement) have very different average sulfate concentrations, the sulfate concentration of a bulk carbonate that consisted only of these two components would be a function of the mixture. In contrast, Fig. DR6B shows a ternary diagram with the calculated sulfate concentration of bulk carbonate comprised of skeletal grains, detrital micrite, and micritic coatings. Since two of these components (detrital micrite and skeletal grains) are similar in their average sulfate concentration, the sulfate concentration of a bulk carbonate that consisted only of these two components would not be a function of the mixture. This does not hold for micritic coatings, which are enriched in sulfate, and the contours on the ternary diagram show that as the proportion of the bulk comprised of micritic coatings increase, the sulfate concentrations increase. Micritic coatings were observed largely at the boundaries of grains, and not in the detrital carbonate, so constant proportions (10 % and 20 %) of micritic coatings relative to skeletal grains are indicated by the solid black lines. Interpreted literally, this suggests that variations in proportions of these three components makes little difference to the bulk carbonate concentration of sulfate (less than 10 or 20 ppm), particularly if the micritic coatings comprises less than 20 % of the rock.

FIGURE CAPTIONS

Figure DR1: Overview optical image through oncoid grainstone featuring locations of sectors mapped (Figs. 2-3, DR2).

Figure DR2: (A) Optical image through dasyclad algae. (B-E) Maps showing the distribution of inorganic sulfate (B), organosulfate (C), distorted sulfate (D), and a composite of these forms (E). The black bar across the maps represents a temporary shutdown of the beam.

Figure DR3: (A) Optical image through a crinoidal packstone (908-1.0) in the Lousy Cove Mb with (B) corresponding sulfide abundances (2472 eV) and (C) sulfate abundances (2482.7 eV).

Figure DR4: Normal probability (quantile-quantile) plots for sulfate concentrations by synchrotron pixel in Sector 1 (Fig 2: ROIs 1-9) and Sector 2 (Fig 3: ROIs 10-19).

Figure DR5: Density plots of the sulfate concentrations reported for each pixel within each ROI for Sector 1 (Fig 2: ROIs 1-9) and Sector 2 (Fig 3: ROIs 10-19). Grey bars represent the proportion of pixels at each sulfate concentration as measured in the raw data. The red line represents the MLE best-fit normal curve to these data. ROI 3 does not have a fit curve since the MLE approach was unable to fit a curve to these data (see supplementary text).

Figure DR6: (A-H) Ternary diagrams with the calculated sulfate concentration of bulk carbonate comprised of three of six components: skeletal grains, nonskeletal grains, detrital micrite,

oncoids, cement, and micritic coatings. Solid lines on (B) are of constant proportion between skeletal grains and micritic coatings.

Table S1: Summary statistics for sulfate concentration data for each ROI. For each sector we report the arithmetic mean (true.mean), standard deviation (true.sd), and the standard error of the mean (true.sem). We also provide estimates of these statistics obtained by maximum likelihood estimation excluding outliers (ml.mean, mle.sd, mle.sem). For each ROI, n is the total number of pixels, and out.n is the number of pixels after removal of outliers.

Table S2: Adjusted p-values for the pairwise comparison of sulfate concentrations of all ROIs within each Sector.

REFERENCES

Balthasar, U., Cusack, M., Faryma, L., Chung, P., Holmer, L.E., Jin, J., Percival, I.G., and Popov, L.E., 2011, Relic aragonite from Ordovician-Silurian brachiopods: Implications for the evolution of calcification: Geology, v. 39, p. 967–970, doi: 10.1130/G32269.1.

Banner, J.L., and Hanson, G.N., 1990, Calculation of simultaneous isotopic and trace element variations during water-rock interaction with applications to carbonate diagenesis: Geochimica Cosmochimicha Acta, v. 54, p. 3123–3137.

Brand, U., and Veizer, J., 1981, Chemical diagenesis of a multicomponent carbonate system - 1: stable isotopes: Journal of Sedimentary Petrology, v. 51, p. 987–997.

Cusack, M., Dauphin, Y., Cuif, J.-P., Salomé, M., Freer, A., and Yin, H., 2008, Micro-XANES mapping of sulphur and its association with magnesium and phosphorus in the shell of the brachiopod, Terebratulina retusa: Chemical Geology, v. 253, p. 172–179, doi: http://dx.doi.org/10.1016/j.chemgeo.2008.05.007.

Delignette-Muller, M.L., and Dutang, C., 2015, **fitdistrplus** : An *R* Package for Fitting Distributions: Journal of Statistical Software, v. 64, doi: 10.18637/jss.v064.i04.

Desrochers, A., Farley, C., Achab, A., Asselin, E., and Riva, J.F., 2010, A far-field record of the end Ordovician glaciation: The Ellis Bay Formation, Anticosti Island, Eastern Canada: Palaeogeography, Palaeoclimatology, Palaeoecology, v. 296, p. 248–263, doi: 10.1016/j.palaeo.2010.02.017.

Evans, J., 2018, X-ray Absorption Spectroscopy for the Chemical and Material Sciences: John Wiley and Sons, 224 p.

Fernández-Díaz, L., Fernández-González, Á., and Prieto, M., 2010, The role of sulfate groups in controlling $CaCO_3$ polymorphism: Geochimica et Cosmochimica Acta, v. 74, p. 6064–6076, doi: http://dx.doi.org/10.1016/j.gca.2010.08.010.

Gill, B.C., Lyons, T.W., and Frank, T.D., 2008, Behavior of carbonate-associated sulfate during meteoric diagenesis and implications for the sulfur isotope paleoproxy: Geochimica et Cosmochimica Acta, v. 72, p. 4699–4711, doi: http://dx.doi.org/10.1016/j.gca.2008.07.001.

Gruzensky, P.M., 1967, Growth of calcite crystals, *in* Peiser, H.S. ed., Crystal Growth, Pergamon, p. 367.

Jones, D.S., and Fike, D.A., 2013, Dynamic sulfur and carbon cycling through the end-Ordovician extinction revealed by paired sulfate-pyrite $\delta^{34}S$: Earth and Planetary Science Letters, v. 363, p. 144–155.

Jones, D.S., Fike, D.A., Finnegan, S., Fischer, W.W., Schrag, D.P., and McCay, D., 2011, Terminal Ordovician carbon isotope stratigraphy and glacioeustatic sea-level change across Anticosti Island (Québec, Canada): Geological Society Of America Bulletin, v. 123, p. 1645–1664.

Jugo, P., Wilke, M., and E. Botcharnikov, R., 2010, Sulfur K-edge XANES analysis of natural and synthetic basaltic glasses: Implications for S speciation and S content as function of oxygen fugacity: v. 74, 5926-5938 p., doi: 10.1016/j.gca.2010.07.022.

Long, D.G.F., 2007, Tempestite frequency curves: a key to Late Ordovician and Early Silurian subsidence, sea-level change, and orbital forcing in the Anticosti foreland basin, Quebec, Canada: Canadian Journal of Earth Sciences, v. 44, p. 413–431, doi: 10.1139/e06-099.

Long, D.G.F., and Copper, P., 1987, Late Ordovician sand-wave complexes on Anticosti Island, Quebec: a marine tidal embayment? Canadian Journal of Earth Sciences, v. 24, p. 1821–1832, doi: 10.1139/e87-173.

Okude, N., Nagoshi, M., Noro, H., Baba, Y., Yamamoto, H., and Sasaki, T.A., 1999, P and S K-edge XANES of transition-metal phosphates and sulfates: Journal of Electron Spectroscopy and Related Phenomena, v. 101–103, p. 607–610, doi: 10.1016/S0368-2048(98)00341-7.

Paquette, J., and Reeder, R.J., 1990, New type of compositional zoning in calcite: Insights into crystal-growth mechanisms: Geology, v. 18, p. 1244 LP-1247, http://geology.gsapubs.org/content/18/12/1244.abstract.

Perrin, J., Rivard, C., Vielzeuf, D., Laporte, D., Fonquernie, C., Ricolleau, A., Cotte, M., and Floquet, N., 2017, The coordination of sulfur in synthetic and biogenic Mg calcites: The red

coral case: Geochimica et Cosmochimica Acta, v. 197, p. 226–244, doi: http://dx.doi.org/10.1016/j.gca.2016.10.017.

Petryk, A.A., 1981, Stratigraphy, sedimentology and paleogeography of the Upper Ordovician–Lower Silurian of Anticosti Island, Quebec, *in* Lesperance, P.J. ed., Field Meeting: Anticosti-Gaspe, Quebec, International Union of Geological Sciences, p. 11–39.

Present, T.M., Paris, G., Burke, A., Fischer, W.W., and Adkins, J.F., 2015, Large Carbonate Associated Sulfate isotopic variability between brachiopods, micrite, and other sedimentary components in Late Ordovician strata: Earth and Planetary Science Letters, v. 432, p. 187–198.

R Core Team, 2016, A Language and Environment for Statistical Computing. R Foundation for Statistical Computing, Vienna, Austria: https://www.R-project.org/.

Sami, T., and Desrochers, A., 1992, Episodic sedimentation on an early Silurian, storm-dominated carbonate ramp, Becscie and Merrimack formations, Anticosti Island, Canada: Sedimentology, v. 39, p. 355–381, doi: 10.1111/j.1365-3091.1992.tb02122.x.

Staudt, W.J., Reeder, R.J., and Schoonen, M.A.A., 1994, Surface structural controls on compositional zoning of SO^{2-}_4 and SeO^{2-}_4 in synthetic calcite single crystals: Geochimica et Cosmochimica Acta, v. 58, p. 2087–2098, doi: https://doi.org/10.1016/0016-7037(94)90287-9.

Tamenori, Y., Yoshimura, T., Luan, N.T., Hasegawa, H., Suzuki, A., Kawahata, H., and Iwasaki, N., 2014, Identification of the chemical form of sulfur compounds in the Japanese pink coral (Corallium elatius) skeleton using μ-XRF/XAS speciation mapping: Journal of Structural Biology, v. 186, p. 214–223, doi: http://dx.doi.org/10.1016/j.jsb.2014.04.001.

Webb, S.M., 2005, SIXpack: a graphical user interface for XAS analysis using IFEFFIT: Physica Scripta, v. 2005, p. 1011, http://stacks.iop.org/1402-4896/2005/i=T115/a=305.

Webb, S.M., 2011, The MicroAnalysis Toolkit: X-ray Fluorescence Image Processing Software: AIP Conference Proceedings, v. 1365.

Fig. DR1

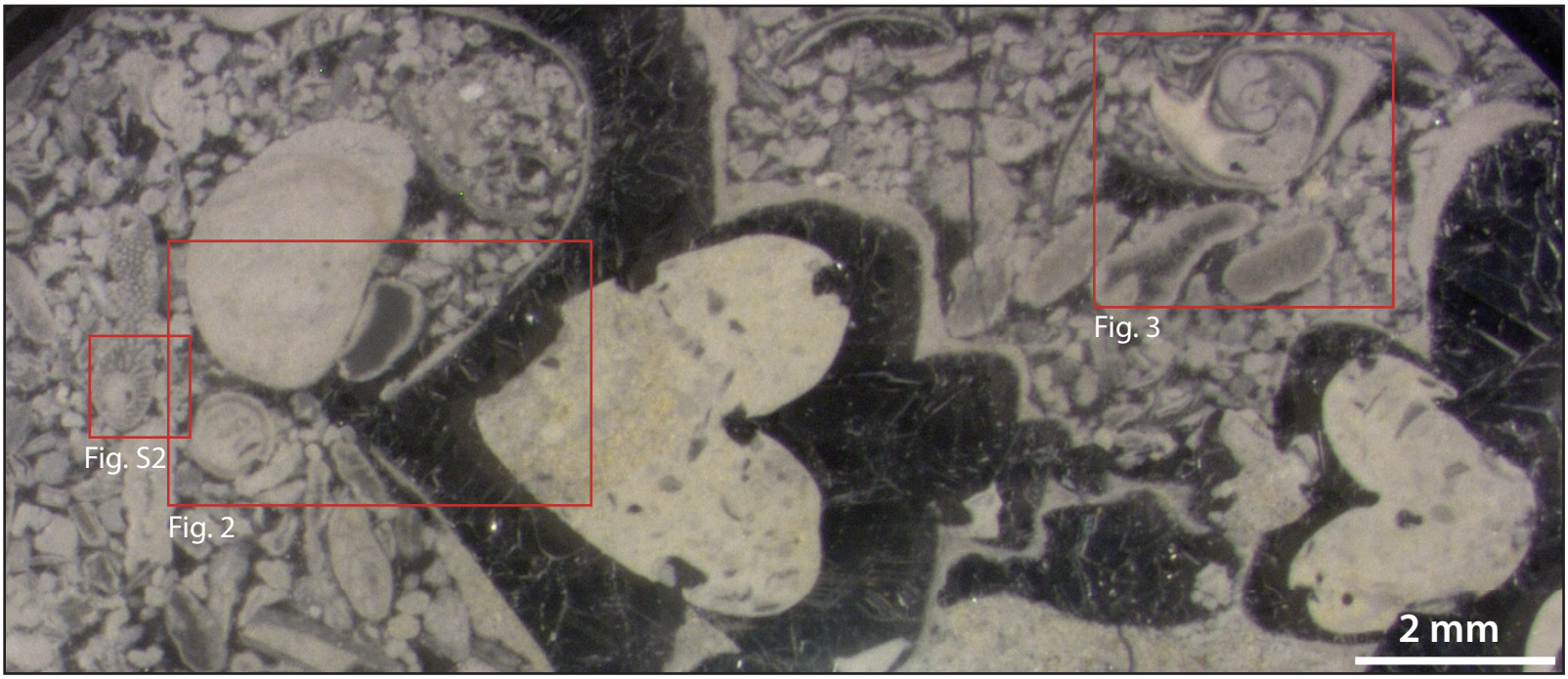

Fig. DR2

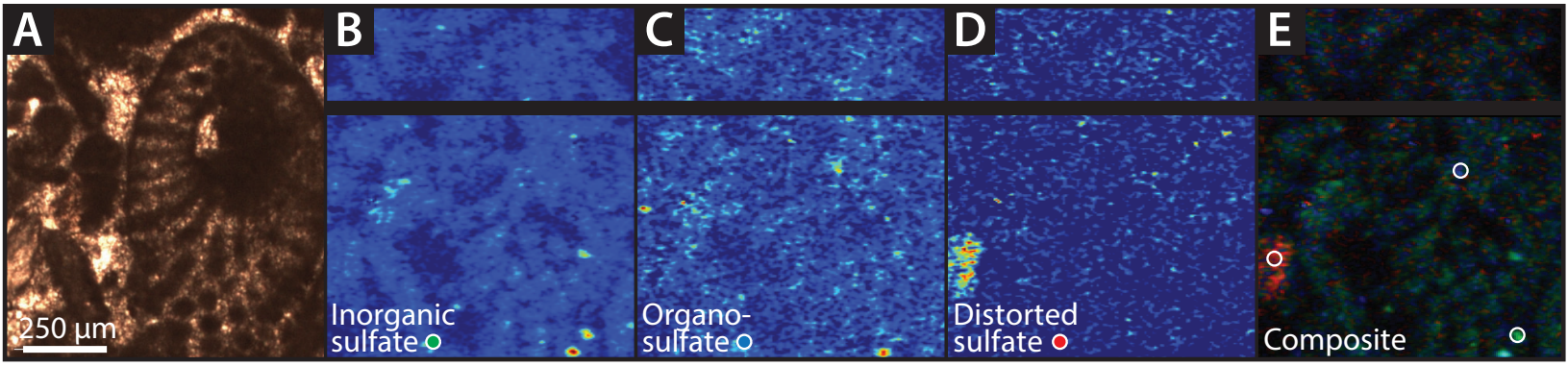
A
B
C
D
E
250 µm
Inorganic sulfate
Organo-sulfate
Distorted sulfate
Composite

Fig. DR3

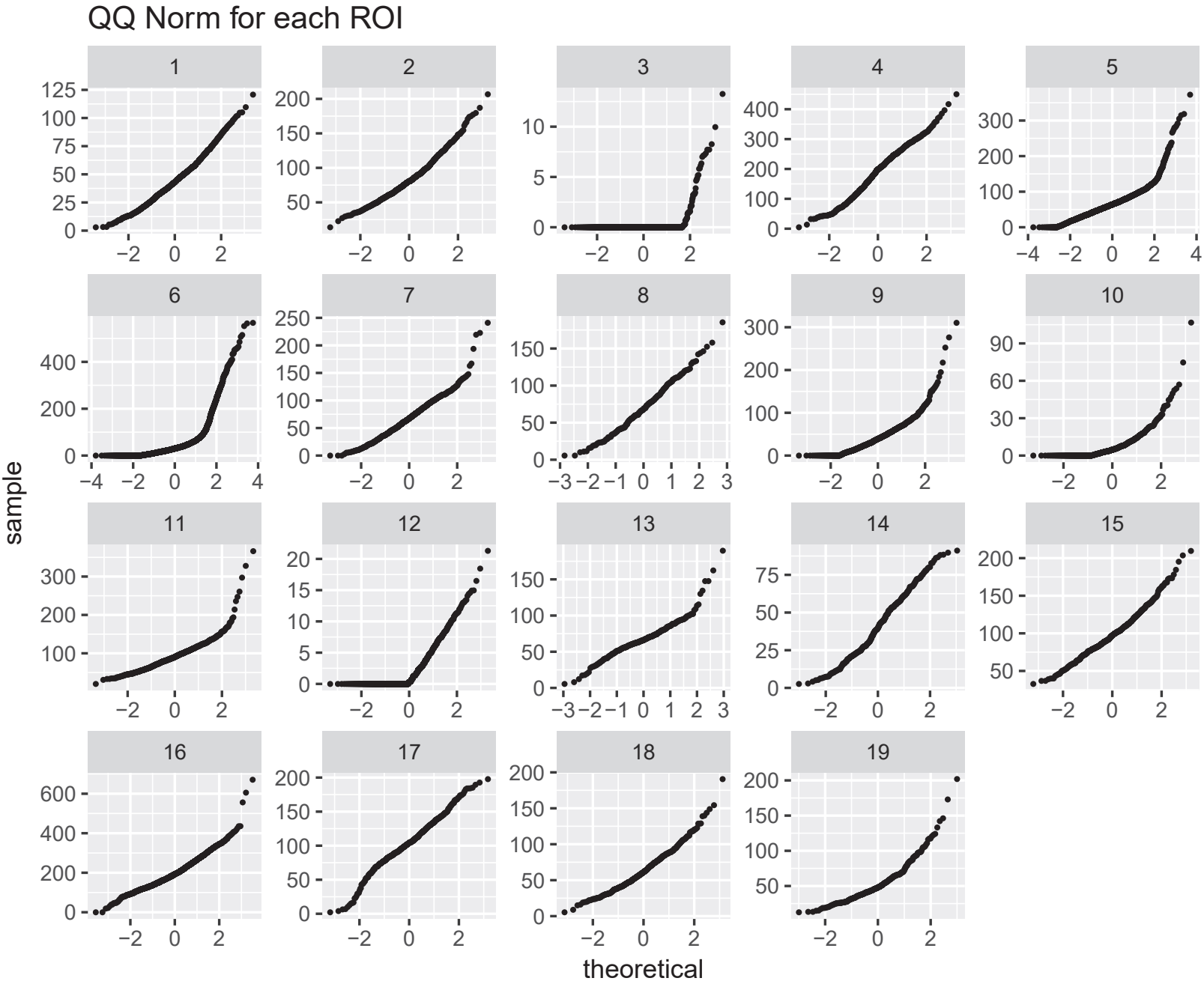
QQ Norm for each ROI
1
2
3
4
5
6
7
8
9
10
11
12
13
14
15
16
17
18
19
sample
theoretical

Fig. DR4

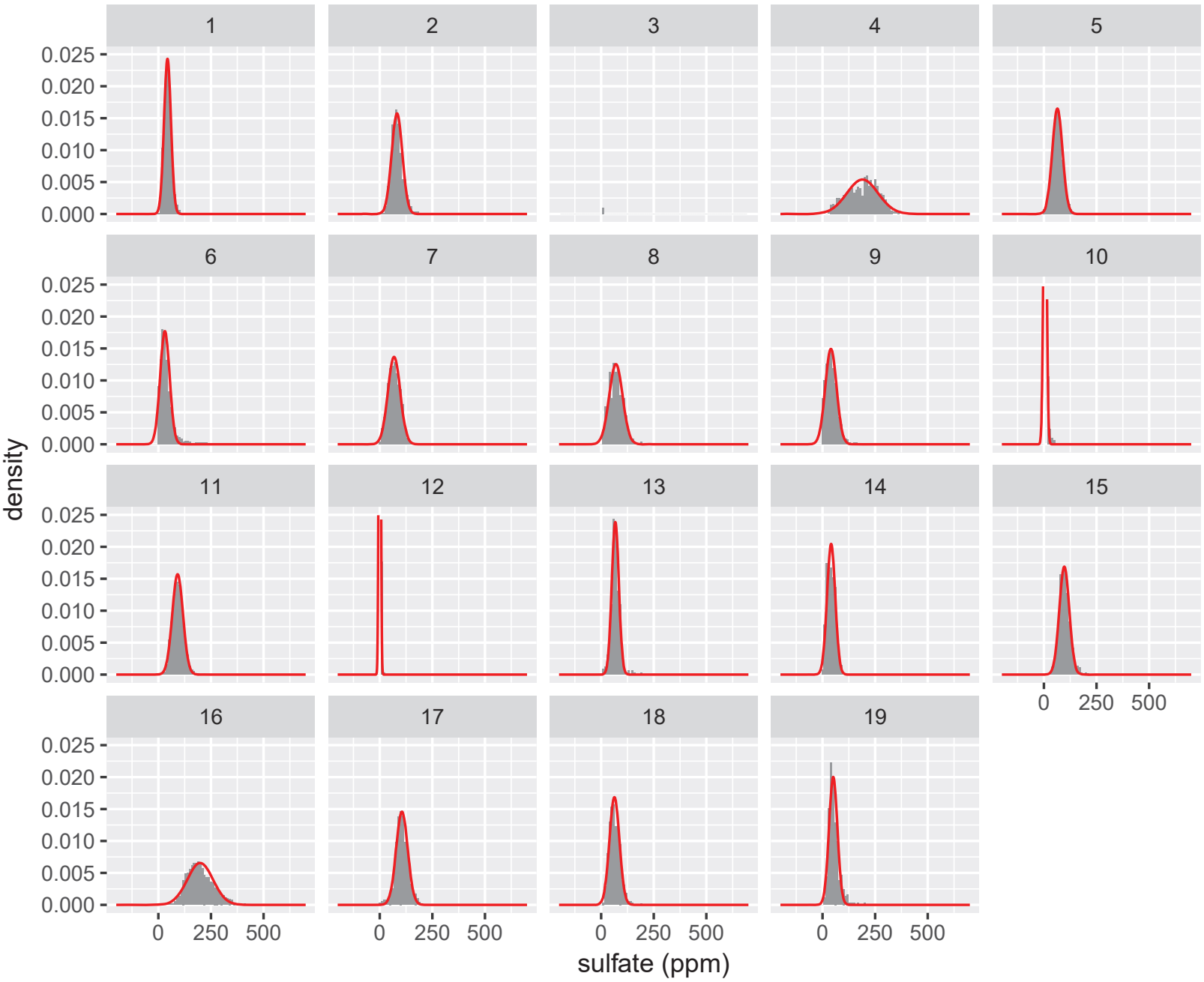
1
2
3
4
5
6
7
8
9
10
11
12
13
14
15
16
17
18
19
density
0.025
0.020
0.015
0.010
0.005
0.000
0
250
500
sulfate (ppm)

Fig. DR5

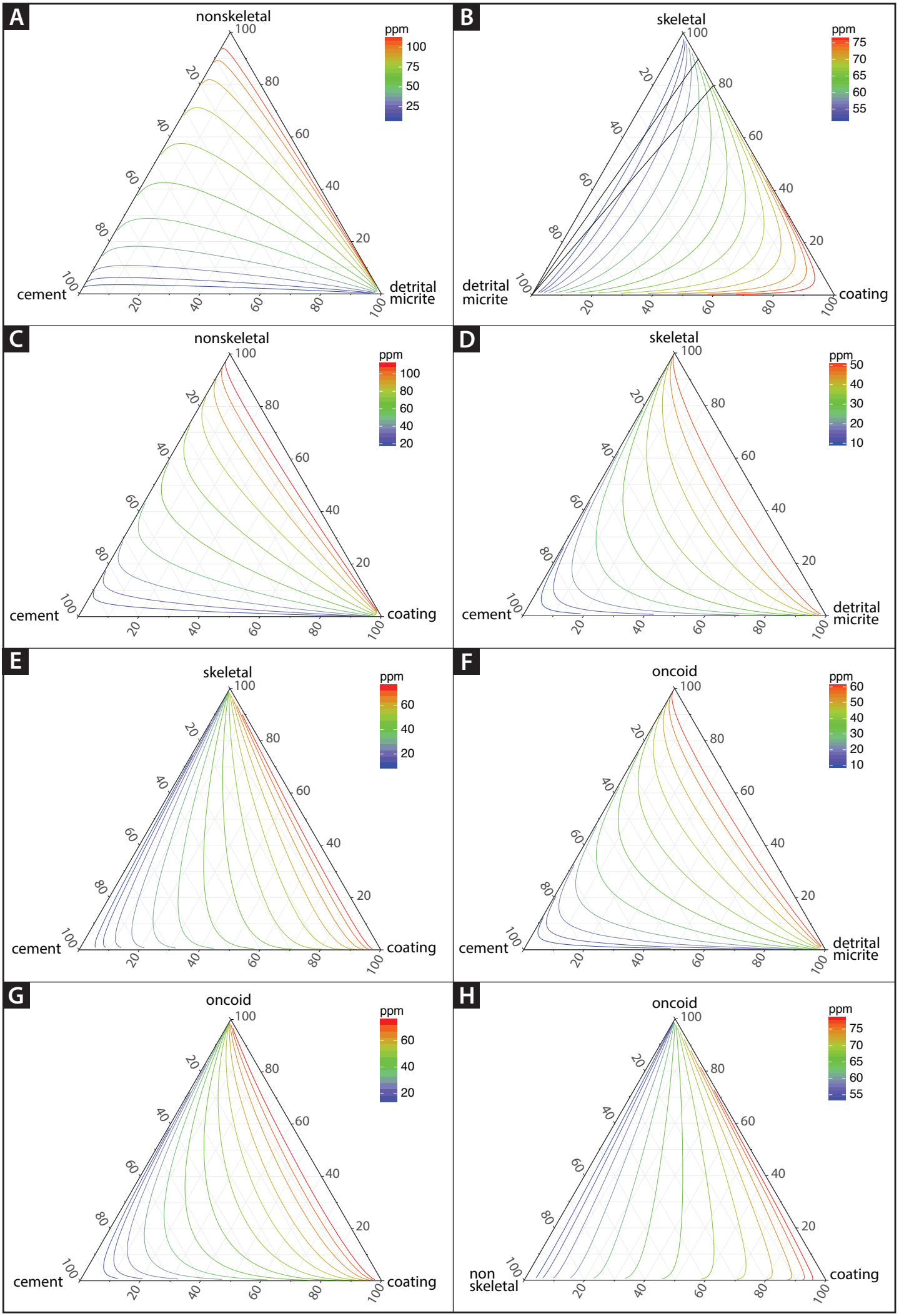
A
nonskeletal
ppm
100
75
50
25
cement
detrital micrite
B
skeletal
ppm
75
70
65
60
55
detrital micrite
coating
C
nonskeletal
ppm
100
80
60
40
20
cement
coating
D
skeletal
ppm
50
40
30
20
10
cement
detrital micrite
E
skeletal
ppm
60
40
20
cement
coating
F
oncoid
ppm
60
50
40
30
20
10
cement
detrital micrite
G
oncoid
ppm
60
40
20
cement
coating
H
oncoid
ppm
75
70
65
60
55
non skeletal
coating

Fig. DR6

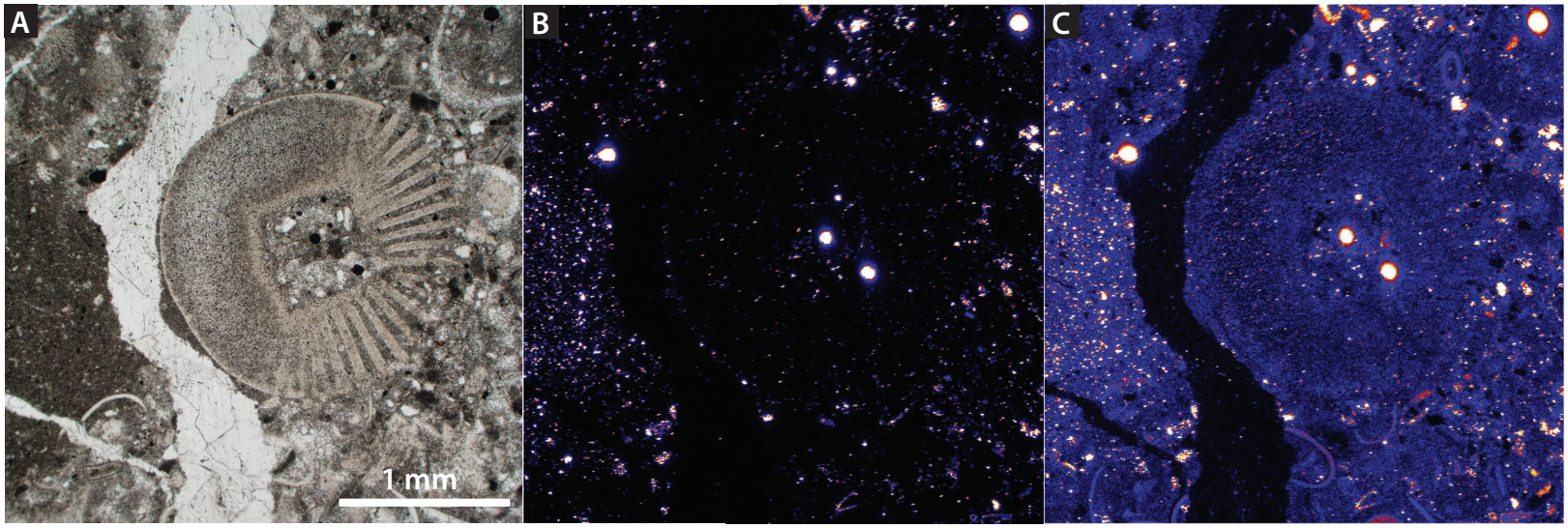

Table DR1

roi	sector	true.mean	true.sd	true.sem	mle.mean	mle.sd	mle.sem	n	out.n
1	1-heart	44.3289988	17.7405809	0.45280754	43.3952594	16.4184289	0.42279606	1535	1508
2	1-heart	83.3791395	27.5768514	0.96185315	81.9642112	25.3329404	0.89065875	822	809
3	1-heart	0.13077748	0.84813638	0.02202395	NA	NA	NA	1483	NA
4	1-heart	190.53919	74.8071955	2.55238857	189.969687	73.9101173	2.52472151	859	857
5	1-heart	66.3230708	29.3098696	0.38958809	64.1118221	24.1755558	0.32448218	5660	5551
6	1-heart	44.4864923	56.4668045	0.68867078	30.9179041	22.5284695	0.28588139	6723	6210
7	1-heart	68.8496918	30.8811414	0.97850641	68.0201874	29.1573167	0.92668036	996	990
8	1-heart	70.6709512	32.7167052	2.20575982	70.1469089	31.7799675	2.1474912	220	219
9	1-heart	43.3650611	32.0220475	0.91678855	39.8885133	26.7161479	0.77413724	1220	1191
10	2-anvil	7.57898572	9.58406658	0.33327065	5.25165081	7.42767748	0.26409781	827	791
11	2-anvil	93.4221539	30.3146709	0.8608788	91.5317135	25.4064522	0.72708668	1240	1221
12	2-anvil	2.23860911	3.28584534	0.10078142	-0.0360417	4.29436147	0.13525967	1063	1008
13	2-anvil	68.056329	21.7452704	1.21559757	67.3270592	16.7052154	0.953417	320	307
14	2-anvil	40.9356744	19.5291934	0.96683914	40.9356744	19.5052459	0.96565356	408	408
15	2-anvil	98.6566268	26.3582758	0.96829546	96.9344222	23.6118592	0.87813449	741	723
16	2-anvil	200.473597	65.2311457	1.26692277	198.561044	60.8267818	1.1881228	2651	2621
17	2-anvil	104.843343	30.9742811	1.19308473	105.503985	27.355566	1.06968728	674	654
18	2-anvil	64.188216	25.4110043	1.08649609	63.203533	23.6601538	1.01722946	547	541
19	2-anvil	53.7569687	25.3854067	1.33055684	50.8020496	19.9226163	1.06339059	364	351

Table DR2

ROI	**1**	**2**	**3**	**4**	**5**	**6**	**7**	**8**	**9**
1	1.00E+00	NA	NA	NA	NA	NA	NA	NA	NA
2	6.66E-256	1.00E+00	NA	NA	NA	NA	NA	NA	NA
3	3.94E-302	4.30E-278	1.00E+00	NA	NA	NA	NA	NA	NA
4	7.89E-216	4.67E-68	2.48E-217	1.00E+00	NA	NA	NA	NA	NA
5	7.83E-252	7.48E-04	1.23E-107	1.03E-25	1.00E+00	NA	NA	NA	NA
6	4.159780e-317	2.00E-150	7.13E-04	1.97E-213	1.37E-106	1.00E+00	NA	NA	NA
7	4.67E-172	5.75E-02	7.28E-26	8.04E-06	1.00E+00	2.47E-30	1.00E+00	NA	NA
8	NA	NA	NA	NA	NA	NA	NA	NA	NA
9	0.00E+00	0.00E+00	2.79E-123	3.47E-302	4.42E-209	4.17E-26	8.16E-45	NA	1

ROI	**10**	**11**	**12**	**13**	**14**	**15**	**16**	**17**	**18**	**19**
10	1.00E+00	NA	NA	NA	NA	NA	NA	NA	NA	NA
11	8.36E-68	1.00E+00	NA	NA	NA	NA	NA	NA	NA	NA
12	3.71E-212	4.30E-73	1.00E+00	NA	NA	NA	NA	NA	NA	NA
13	6.10E-227	3.87E-91	2.22E-05	1.00E+00	NA	NA	NA	NA	NA	NA
14	5.09E-134	2.11E-200	0.00E+00	0.00E+00	1.00E+00	NA	NA	NA	NA	NA
15	0.00E+00	0.00E+00	0.00E+00	0.00E+00	0.00E+00	1	NA	NA	NA	NA
16	1.64E-151	6.35E-202	0.00E+00	0.00E+00	8.17E-65	0	1.00E+00	NA	NA	NA
17	7.21E-247	2.28E-118	1.71E-25	5.98E-09	0.00E+00	0	0.00E+00	1.00E+00	NA	NA
18	1.93E-49	3.06E-02	2.14E-93	8.40E-112	1.15E-240	0	1.71E-252	3.58E-139	1.00E+00	NA
19	1.24E-10	3.92E-28	5.30E-141	1.73E-158	5.47E-150	0	1.71E-161	7.75E-184	9.86E-16	1